AAS 16-256

PRELIMINARY INVESTIGATION OF ONBOARD ORBIT DETERMINATION USING DEEP SPACE ATOMIC CLOCK BASED RADIO TRACKING

Todd A. Ely[*], Jeanette Veldman[†], Jill Seubert[‡]

The Deep Space Atomic Clock mission is developing a small, mercury ion atomic clock with Allan deviation of less than 1e-14 at one day (current estimates < 3e-15) for a yearlong space demonstration beginning late-2016/early-2017. DSAC's stability yields one-way radiometric data precision on par with current two-way data. Uplink one-way tracking with an appropriately configured radio enables the possibility of onboard, autonomous radio navigation. This study examines the modeling needed to efficiently process this data for an onboard implementation.

INTRODUCTION

Routine use of one-way radiometric tracking for navigation and radio science is not possible today because the state of the art spacecraft frequency and time references, ultra stable oscillators, introduce significant error in the data from their intrinsic drift and instability on timescales past 100 seconds. The Deep Space Atomic Clock (DSAC), currently under development as a NASA Technology Demonstration Mission, is a space-flight suitable, mercury-ion atomic clock that provides an unprecedented frequency and time stability that enables routine use of one-way radiometric signals for deep space navigation and radio science.

Ground-based atomic clocks are the cornerstone of spacecraft navigation for most deep space missions because of their use in forming precision two-way coherent Doppler and range measurements. DSAC will provide an equivalent capability onboard a spacecraft for forming precision one-way radiometric tracking data (i.e., range, Doppler, and phase). With an Allan deviation (AD) at one day of better than 1e-14, DSAC will have a long-term accuracy and stability that is equivalent to the existing Deep Space Network (DSN) atomic clocks. Indeed, ground-based testing of the DSAC mission's flight demonstration unit is exhibiting ADs of better than 3e-15 at a day. By virtually eliminating spacecraft clock errors from tracking data, DSAC enables a shift to a more efficient, flexible, and extensible one-way tracking architecture.

---

[*] Principal Investigator, Deep Space Atomic Clock Technology Demonstration Mission, Jet Propulsion Laboratory, California Institute of Technology, MS 301-121, 4800 Oak Grove Drive, Pasadena, CA, 91109-8099; Todd.A.Ely@jpl.nasa.gov, 818-393-1744.

[†] Graduate student, University of Colorado, Aerospace Engineering Sciences, Engineering Center ECOT-634, 1111 Engineering Drive, Boulder, CO, 80309-0429

[‡] DSAC Investigation System Engineer, Jet Propulsion Laboratory, California Institute of Technology, MS 301-121, 4800 Oak Grove Drive, Pasadena, CA, 91109-8099

© 2016. All rights reserved.

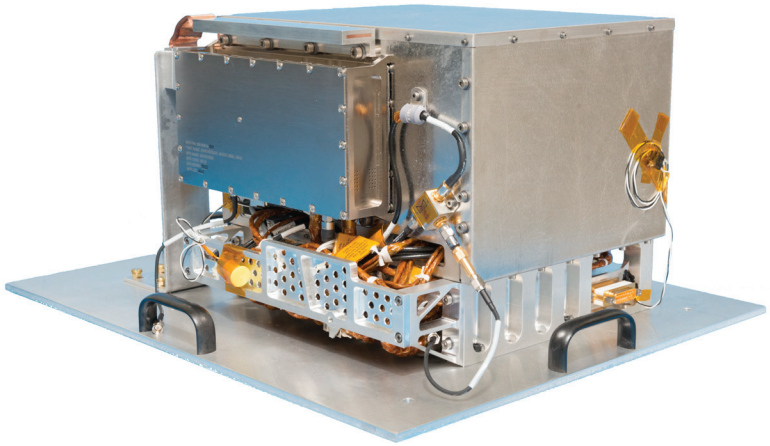

Figure 1: The DSAC Demonstration Unit (sitting on top of a plate for ease of transportation).

The DSAC project is currently building a demonstration unit of the atomic clock (see Figure 1) that will be launched into low Earth orbit between late-2016 and early-2017 for a yearlong demonstration of its functionality and utility for one-way based navigation. This will bring the technology to a Technology Readiness Level (TRL) 7, and ready it for infusion into a planetary science mission where the development focus would shift from fundamental technology issues to optimizing the clock for extended operational use.

A DSAC-equipped spacecraft tracking a one-way uplink with its radio receiver could self-navigate in deep space if this data is processed by a capable onboard navigation system. In this paper we begin investigating key facets of autonomous navigation using one-way radiometric measurements. Simulations of one-way radiometric tracking using DSAC have already been shown to produce accurate orbit solutions using high fidelity models [1]. The challenge for an onboard navigation system is designing the trajectory modeling, estimators, and solution assessment algorithms so that they work well with the limited computational resources that are available on a spacecraft. With this in mind, a first step towards designing such a system is to investigate reduced-order models that are sufficient for meeting desired navigation requirements while minimizing the computational burden needed to compute the solutions. This should be contrasted with ground-based navigation systems that strive for the highest fidelity model and solution algorithms because computational speed and resources are not a limiting factor in performance. Specifically, orbit determination for a typical Mars low-altitude orbiter has been selected as a representative use case. The following issues are examined:

- Identify simplified gravity models, spacecraft shape models, and non-gravitational acceleration models (such as atmospheric drag) that reduce processing time.
- Examine linearized and extended Kalman filtering for its utility in onboard processing. Particular attention is focused on issues of linearity and solution biasing.

Preliminary results indicate that significant model simplifications can be obtained while still maintaining accurate solutions. An example is to replace the typical multi-component, attitude dependent shape models often used in ground-based processing with a simple spherical spacecraft shape model. These and other model simplifications are examined in this paper.

UPLINK ONE-WAY RADIOMETRIC TRACKING WITH DSAC

DSAC enables a shift to a one-way radiometric tracking architecture from the two-way architecture provided today by the DSN. This has the potential to not only increase the amount of

© 2016. All rights reserved.

tracking data, but also the quality of that data. A scalable one-way tracking architecture offers the possibility to navigate in new and different ways, including the potential for autonomous radio navigation.

With DSAC and a suitably-configured radio onboard a spacecraft, one-way range and Doppler measurements could be collected for immediate use in a real-time autonomous navigation system. Because of DSAC's stability and accuracy the measured data is as accurate as would be obtained if the signal were coherently transponded and collected back at Earth using traditional two-way tracking techniques [1].

Another benefit of uplink one-way radiometric tracking is that the signal power required to track is significantly reduced as compared to a two-way link. This enables a spacecraft to utilize much lower gain antennas for tracking, which provide more hemispherical coverage relative to their higher gain counterparts. Additionally, most spacecraft employ low gain antennas in each discrete spacecraft-fixed direction (i.e., one on each X, Y, and Z oriented face) to provide full Earth coverage in the event of spacecraft faults or compromised communications. Coupling low power requirements with hemispherical low gain coverage implies one-way tracking with DSAC yields more actual tracking data in most operational situations (for instance, science orbits with constrained attitudes to support science instrument coverage) relative to two-way tracking that requires higher gain antennas (often gimbaled) to get equivalent tracking.

A DSAC-enabled spacecraft tracking a one-way uplink transmission using an onboard receiver could self-navigate in deep space using this data combined with a capable navigation system. Aspects of deep space navigation autonomy have been demonstrated using optical navigation with the Deep Space 1 (DS1), Deep Impact, and Stardust missions [2]–[4]. However, a complete implementation of a fully autonomous onboard navigation system would couple a DSAC-enabled one-way uplink (or forward link) radiometric tracking system with optical tracking from a camera system. This would combine the strengths of radio navigation for determining absolute location in deep space and in planetary orbits with the target relative navigation provided by the optical system. A combined one-way radiometric and optical autonomous navigation system would provide a powerful solution for robotic missions where ground-in-the-loop operations are infeasible (deep space encounters, planetary capture, real-time orbital operations, etc.), as well as supporting human exploration missions beyond low Earth orbit that require crewed operations without ground support.

MODEL CONSIDERATIONS FOR ONBOARD ORBIT DETERMINATION AT MARS

A complete study of deep space autonomous navigation will be a complex and lengthy investigation. The current effort begins by first determining what model fidelity is sufficient for onboard orbit determination (OD) in a compelling use case. We have picked a low altitude Mars orbiter for this case as there are five orbiters at Mars now and others are envisioned including the Mars 2022 orbiter currently being planned by NASA. Furthermore, human exploration of the solar system has set Mars in its sights and will eventually lead to crewed missions orbiting and landing at Mars. These missions will have need for autonomous navigation and as a first step, understanding the relationship between model fidelity and orbit solution accuracy is needed.

As just discussed, this onboard navigation is enabled via one-way uplink tracking of radio signals and to ensure accurate data; DSAC would be needed as the reference oscillator for the spacecraft receiver. A detailed investigation into the characteristics of this data was documented by Ely [5] and will not be repeated here. Key considerations for use of this data are ensuring the orbit determination filter properly accounts for frequency and time offsets and calibration models exist for correcting phase/temperature effects induced by the receiver. These issues will be delineated as needed in the context of the low Martian orbit OD problem being studied.

© 2016. All rights reserved.

We will be studying model adaptations to the high fidelity models routinely used for operational OD of current Mars orbiting missions that simplify the computations (and potentially processing speed) while minimizing the degradation in overall performance. The objective is to determine which dynamic and measurement models can be simplified or negated while still satisfying a mission's navigation requirements. For the Mars orbiter case study, the one-sigma OD reconstruction requirements are

1. 0.5m in the radial direction,
2. 33m in the transverse direction, and
3. 13m in the cross-track direction.

These requirements have been used by the MRO mission, while they are not necessarily the requirements for future Mars orbiting missions they do provide reasonable targets with which to search for a sufficient set of model simplifications.

We'll examine three key model simplifications that would be prudent for reducing the complexity of an onboard orbit determination capability – reduction of the necessary gravity field degree and order, simplify the spacecraft shape modeling for solar pressure and drag, and reduce the fidelity of the atmospheric density model. We will also begin to explore an extended Kalman filter approach as compared to the traditional iterated, linearized Kalman filter typically used during operations.

Truth Trajectory, Measurement Modeling, and Baseline (Full Fidelity) Solution

Our filter study will simulate a high fidelity 'truth' trajectory and corresponding Doppler and range data for a low altitude Mars orbiter for a 4-day period. The truth scenario is configured to mimic Mars Reconnaissance Orbiter (MRO) operational navigation and gravity field reconstruction, but adapted for one-way radiometric data processing [6], [7]. The simulated Mars orbiter is placed in a near-polar, sun-synchronous orbit with a 3656 km semi-major axis and eccentricity of 0.0055. The initial state was propagated including the dynamical effects of solar pressure, Mars atmosphere using the 2005 Mars Global Reference Atmospheric Model (MarsGRAM 2005) [8], a 95x95 spherical harmonic Mars gravity field, third body gravity for the sun, moon, and planets all including relativistic effects. The orbital dynamics model included a 10% random bias on the solar pressure scale factor and a 10% first order Gauss-Markov stochastic process (or exponentially correlated random variable – ECRV) on nominal Martian atmospheric density scale factor. Furthermore, the truth shape and reflection models for the orbiter use the high fidelity operational configuration that has been developed over the past decade by the MRO operational navigation team. Finally, for reasons that will be discussed shortly, the initial state was randomly perturbed from nominal with a 5 cm (1σ) position error and a 0.05 mm/s (1σ) velocity error. The resulting truth trajectory spans February 28, 2015 05:50:00.00 ET to March 4, 2015 05:05:00.00 ET.

Because of the significant number of missions at Mars, it is reasonable to assume that at any time at least one DSN antenna is pointed towards the planet. Additionally, in this study, the orbiter's receiver is configured to collect one-way range and Doppler using DSAC as its reference.[*] Thus accurate one-way uplink-only tracking data is available continuously, except during occultations, for processing by the onboard navigation system. Doppler and range X-band measurements were generated from the truth trajectory and consistent with the geometrically viable viewing opportunities. In addition to using the truth trajectory, high fidelity measurement models were used

[*] Currently most Mars missions use the Small Deep Space Transponder that is not capable of collecting range or Doppler. However, the Unified Space Transponder being currently developed by JPL is planned to have the ability to collect and/or generate one-way radiometric signals.

© 2016. All rights reserved.

Table 1: Baseline Mars Orbiter Simulation Error & Filter Configuration

Parameter	**Simulation Error (1σ Gaussian draws unless stated otherwise)**	**Filter Type**	***A Priori* Uncertainty/ Noise Strength**
Position Components	5 cm	Dynamic	100 km
Velocity Components	5 mm/s	Dynamic	10 m/sec
Solar Pressure Scale	10%	Bias	10%
Drag Scale	ECRV, 10% steady state, ¼ sol correlation	ECRV	10% steady state, ¼ sol correlation
Mars GM	nominals	Bias	5 x 0.000024 km^3/sec^2
Mars J_{12} Mars J_{13}	nominals nominals	Bias Bias	5 x 0.23e-10 5 x 0.25e-10
Range Bias	2 m applied at start of each pass	Per-Pass Stochastic	2 m
Clock Bias	1.e-3 sec	Bias	1 sec
Frequency Bias	1.e-9	Bias	0.1
Stochastic Frequency	White Frequency (WF) Noise Sequence with A.D. = 3.e-15 @ 1-day	WF Process	3.e-15 @ 1-day
Earth troposphere and ionosphere delays	Observed values	N/A	N/A

that account for extended signal transit times (i.e., light time delays) and all relativistic effects including the impacts to a Mars orbiting clock. Gaussian noise degradation of the measurements was performed at the traditionally utilized 0.1 mm/sec (X-band). Clock noise was also incorporated into the measurements in order to reflect the stochastic clock behavior of the onboard frequency reference, DSAC. The DSAC stochastic model is a white frequency noise sequence simulated in accordance with DSAC's current best estimate (CBE) performance of 3.e-15 at one day. Finally, range biases, troposphere and ionosphere delays were added to the measurements at levels consistent with observed values over the simulation epochs.

The baseline, full-fidelity orbit determination filter was configured in a manner similar to MRO ground 1operations but adapted to account for processing one-way uplink radiometric data (versus the normal two-way DSN radiometric data collected back at Earth). The simulation errors, filter setup and associated *a priori* uncertainty values are summarized in Table 1. The filter is a batch sequential linearized Kalman filter (LKF) using a UD factorization to ensure numerical stability. This is the filter type that is typically selected for operations. The estimated filter states included the inertial position and velocity of the orbiter, solar pressure and atmospheric drag scale factors, and J_{12} and J_{13} Martian gravity biases [6], [7]. The solar pressure scale factor was estimated as a constant bias, while the drag scale factor was estimated as an ECRV. Processing one-way Doppler and range tracking data requires estimating additional clock bias, frequency states, and range biases. Finally, all of the Earth atmosphere delays from the troposphere and ionosphere are injected into the truth measurements, and during analysis the computed measurements have not been calibrated for these delays. Thus, all media delays represent an unmodeled error source.

A simulation of the expected baseline results are shown in Figure 2 and demonstrate the solution errors and uncertainties with the results achieving meter level positioning performance.

© 2016. All rights reserved.

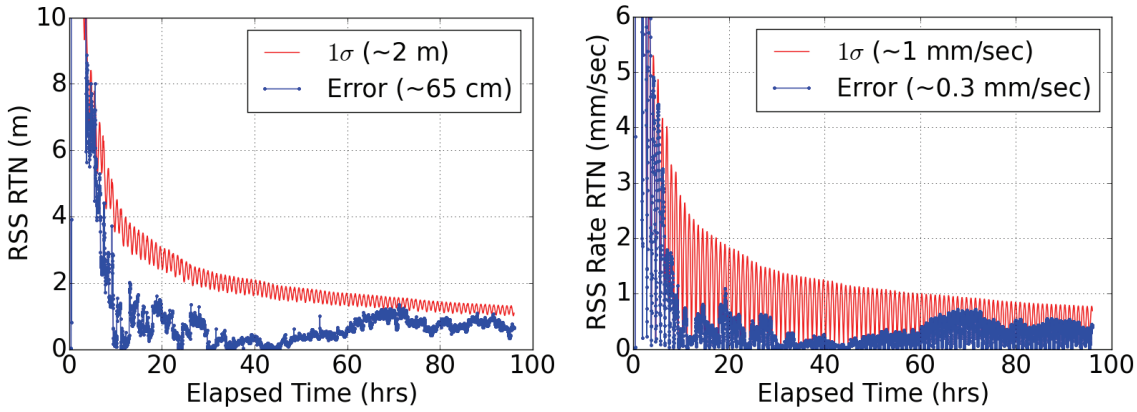

Figure 2: Baseline orbit solution errors and uncertainties with full fidelity models. Steady state errors and uncertainties computed using results in the last 20 to 48 hrs.

The steady state root mean square (RMS) uncertainties and errors are determined by computing the statistics using all data after the first 20 hours to ensure that the bulk of the filter's transient effects have diminished. As the models are simplified, these results represent the baseline from which to measure deviations. They also demonstrate that processing DSAC-based one-way radiometrics yields orbit solutions that are as accurate as would have been obtained via processing two-way data [1]. The overall, steady state RMS position error is 52 cm and velocity error at 0.2 mm/sec with the associated uncertainties at 2 m and 0.4 mm/sec, respectively. These results meet the orbit accuracy requirements with healthy margins, and suggest opportunities for model simplification exist.

Linearized Kalman Filter and Extended Kalman Filter Considerations

As mentioned previously, the simulated initial condition errors were limited to 5 cm (1σ) in each position component, and 5 mm/s (1σ) in each velocity component. This was done because early in this study it was determined that the LKF would yield biased solutions when any appreciable initial condition errors were present. It was ascertained that this scenario, and perhaps most deep space orbit determination problems, are very susceptible to linearization issues associated with initial condition errors. In practice, orbit determination procedures would process a nominal set of data using the LKF, for a Mars orbiter this is traditionally 2 days of tracking, and then iterate the solution several times until convergence to a desired threshold is achieved. In the present case, convergence typically takes three iterations; by comparing with an additional iteration, the trajectory difference yields the 5 cm level position differences and 5 mm/s velocity differences used in this example. Thus, for an LKF implementation to work robustly requires an iterated solution as initial condition errors could be much larger than the 5 cm, 5 mm/s levels. For an onboard application, this could present processing throughput issues as each iteration is a complete processing pass through all of the data. We elected to investigate this issue in two ways, first by exploring model simplifications of the other data types using the LKF but with the 5 cm, 5 mm/s level initial errors, and, secondly, by investigating an Extended Kalman Filter (EKF) approach for solution stability when presented with larger initial errors. In what follows, we'll discuss model simplifications, then address the EKF.

Model Simplifications

The full fidelity MarsGRAM 2005 is a complicated model with a significant number of computations that include a number of tabular interpolations. An empirically derived model, called

© 2016. All rights reserved.

MarsGRAM Simplified or MarsGs for short, derived by Vincent [9], was investigated. It computational complexity is much reduced as compared with MarsGRAM 2005. The MarsGs density ρ can be expressed as

$$\rho(h,t) = \rho_o \exp\left[-\frac{h-h_o}{H}\right] D(t) \tag{1}$$

where ρ_o is the density at height h_o, H is the scale height, and $D(t)$ is a deterministic scale factor related to the long-period solar flux variations (details can be found in References [9]–[11]). We have formed a least squares fit to MarsGRAM 2005 by estimating best fit values for $\{\rho_o, h_o, H\}$ for the epoch and duration selected for the simulation. A true onboard implementation may consider fitting for a much longer period, say three months, so as to minimize the number of times model updates would be required during operations.

Computations were further simplified by representing the spacecraft shape as a sphere. Doing so effectively creates an attitude-free model that eliminates the need to interface with an onboard attitude determination system. Of course, it would be possible to implement such an interface with an actual navigation system, but we wanted to explore how simple of a model could be achieved and still retain sufficiently accurate solutions. The sphere is as simple a model as could be envisioned, as even a flat plate would require some form of attitude information. The procedure to compute a radius for the drag sphere is as follows:

1. The drag acceleration is computed using either the full-fidelity MarsGRAM 2005 density or the MarsGs density along the truth trajectory using the full spacecraft shape model to yield a set of acceleration values $\{a_d(t_i)\}$.
2. A time series of areas $\{A(t_i)\}$ is computed using the constraint equation

$$A = \frac{2a_d m}{\rho C_d v^2} \tag{2}$$

   where m is the spacecraft mass, C_d is the drag coefficient, and v is the Mars relative magnitude of the spacecraft velocity.

3. The average area $\overline{A}$ is computed from the series $\{A(t_i)\}$, and the drag radius is determined via

$$r = \sqrt{\overline{A}/\pi}. \tag{3}$$

This radius applies to the shape for evaluating the drag acceleration. Similarly, a spherical shape model can be used in computing the solar radiation pressure acceleration. The same method was used as with the drag, but now a series of cross-sectional areas are computed using the following constraint equation

$$A = \frac{a_{SRP} m R_S^2}{f C} \tag{4}$$

where a_{SRP} is the solar pressure acceleration obtained from computing the high fidelity solar pressure and shape models, R_S is the distance from the spacecraft to the Sun, f is the shadow factor, and C is the solar flux at 1 au. Again, areas are averaged and the solar pressure spacecraft sphere radius is computed using Eq. (3). Using a sphere to compute the solar pressure introduces an additional error because it cannot capture all components of the force vector. Typically, the solar pressure force includes a component along the Spacecraft-Sun line (as is the case with the sphere) plus another in some other direction that is the aggregate of surface normal forces to each spacecraft

© 2016. All rights reserved.

facet. The sphere cannot capture this last component; however, as will be seen neglecting it introduces a negligible error even for a spacecraft like MRO with large arrays and bus structures (such as a high gain antenna).

Lastly consider the acceleration due to gravity, the components here include: the dominant Mars point mass, distributed body gravity effects (as represented by a $\{m, n\}$ field of spherical harmonics) plus other body perturbations primarily from the Sun, and relativistic effects. While high fidelity ephemerides for other bodies can require significant storage space, it would be needed only if extended durations are required, which would not be typical for an onboard application. Therefore, including the other bodies adds only a modest computational burden. This is also the case for relativistic effects. The primary contributor to computational effort for a low altitude orbiter is in evaluating the spherical harmonics field contributions. The field itself can require significant storage space. Consider that the operational field used for MRO, and the one for used for the truth simulation in this study, is a {95,95} field. Gravity fields are lower triangular in form; thus, this field contains 4560 (= 95 x (95+1)/2) terms. In contrast, a {10,10} field contains only 55 terms yielding a reduction by almost a factor of 83.

The simplification of the dominant acceleration sources due to drag, solar pressure, and gravity have been separately examined. After the effects of each simplification has been determined, they will be collectively analyzed to assess the performance of the end-to-end sub-optimal filter strategy.

Drag Reduced Model Fidelity Results

Two drag cases with simplified models were examined, they include:

1. Drag Case 1: The detailed geometric spacecraft shape is replaced with an attitude-independent sphere and the density is the full fidelity MarsGRAM 2005.
2. Drag Case 2: The spacecraft shape is still replaced with a sphere, and also uses the simplified MarsGs atmospheric density model given in Eq. (1).

Recall, that the truth case uses a high fidelity shape model along with the high fidelity MarsGRAM 2005 atmospheric density model. A time series of the acceleration due to drag for Drag Case 1 is shown in the left plot of Figure 3. The truth scenario is shown in red, while the drag due to a simplified spacecraft spherical shape using the MarsGRAM 2005 density model is presented in blue. The truth acceleration shows an additional peak on each orbit due to attitude-dependent, systematic changes in velocity. The flat plates, solar panels, and the high gain antenna on MRO experience varying drag depending on orientation, not captured when a spacecraft is modelled as a sphere. The acceleration differences between truth and the sphere-based drag, expressed in the wind frame (the wind direction is opposite the Mars relative velocity vector), are shown in the right plot of Figure 3 (note that the horizontal scale is longer in this plot as compared to the left). Although the differences reach only 1e-4 mm/s^2, they are still a sizeable fraction of the absolute magnitude. Nevertheless, as will be seen, properly tuned process noise is still able to maintain filter convergence for acceleration errors of this magnitude without a sizeable increase in solution error relative to the baseline.

© 2016. All rights reserved.

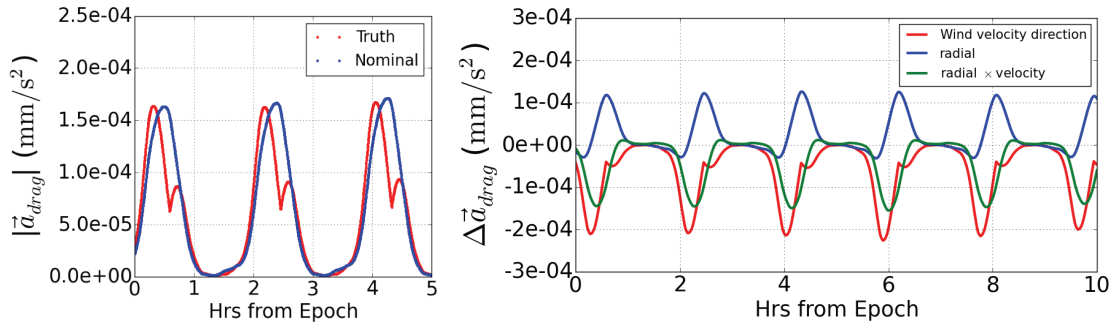

Figure 3: Drag Case 1 (left) accelerations from a spherical s/c shape and MarsGRAM 2005 as compared (red) to truth (blue), and (right) the differences from truth in the wind frame.

In Figure 4, the acceleration magnitude due to drag for Drag Case 2 using a combination of a simplified density and spherical shape is shown in the left plot, again in blue, and the truth scenario acceleration in red. The Drag Case 2 acceleration reaches similar amplitudes as before; however, an additional 'concave' feature can be seen at the beginning of each orbit. An analysis of the trajectory in conjunction with the form of the MarsGs density as given in Eq. (1) reveals that the concavity is due to the exponential relationship between density and altitude. The associated differences between the truth and the sphere-MarsGs-based drag accelerations can be seen in the right plot.

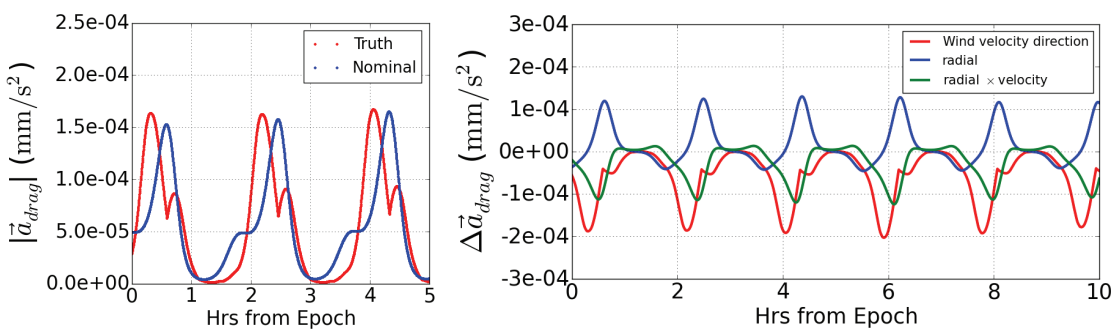

Figure 4: Drag Case 2 (left) accelerations due to spherical s/c shape and the simplified Mars density (MarsGs), and (right) the acceleration differences in the wind frame.

The Allan deviation is a useful statistic for determining the correlation properties on varying timescales of a time series, and the computation of the AD for the two drag cases is shown in Figure 5. Observe that for each case, the Allan deviation reaches a peak at a time interval τ near 1000 seconds and then falls off at about a $1/\tau$ slope; this behavior is indicative of an ECRV process [12]. To account for these effects, the filter process noise model for drag is changed from a stochastic density scale factor parameter that has been optimally tuned for MarsGRAM 2005 to a generic set of three process noise acceleration filter states in the wind-frame that are being driven by ECRV noise with strengths tuned to two times the standard deviation of the acceleration differences. The factor of two was used to ensure the process noise compensates for those drag modeling differences that deviate from an ECRV behavior (i.e., the periodic dips seen in the AD plots in Figure 5 that are indicative of a periodic signal). Furthermore, all the truth model error sources (i.e., the second column in Table 1) were zeroed so that the effect of the filter solution can be examined when only the drag modeling errors are present. Later, when all model reductions have been studied a full simulation with all injected truth errors and model simplifications will be examined.

© 2016. All rights reserved.

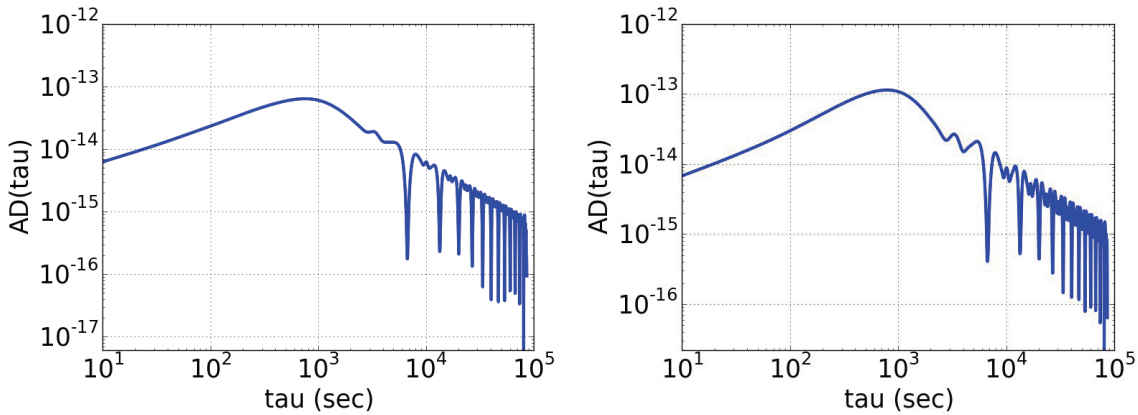

Figure 5: Allan Deviations for Drag Case 1 (left) a spherical shape s/c and MarsGRAM 2005 density, and for Drag Case 2 (right) a spherical shape s/c and MarsGs density.

The root sum of the squares (RSS) filter position solution errors are shown in Figure 6, along with the root mean square (RMS) of the filter solution errors (excluding errors before steady state that is achieved after 20 hours). Drag Case 1 (spherical shape only) had a position error RMS of 35cm, and Drag Case 2 (shape and model simplifications) had a RMS of 40cm. These results illustrate that generic acceleration process noise states can effectively 'absorb' intentional mis-modeling errors (here the shape and density model simplifications). In this first study, the factor of two multipliers on the process noise states yielded satisfactory results; however, it might not be necessary.

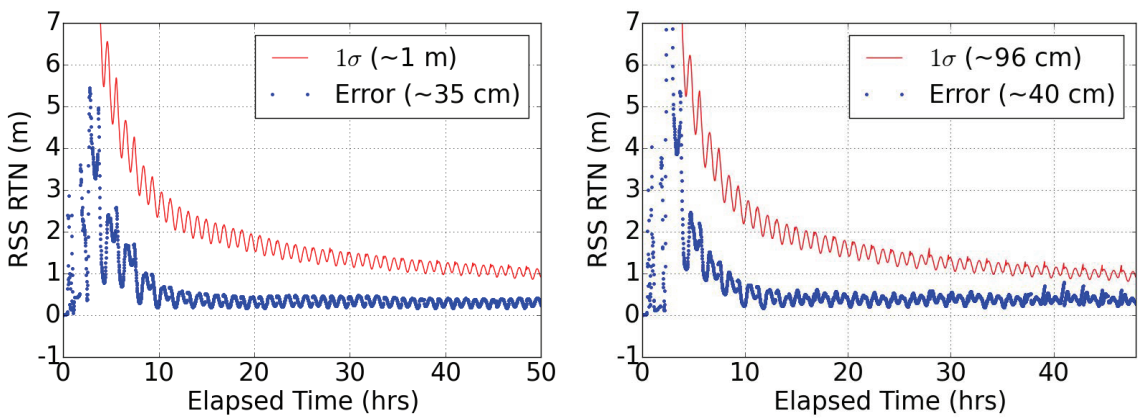

Figure 6: Filter position errors and uncertainties for Drag Case 1 (left) spherical model and MarsGRAM 2005, and for Drag Case 2 (right) spherical model and MarsGs

Solar Radiation Pressure Reduced Model Fidelity Results

The only variable component in the solar radiation pressure model investigated in this study was the area of the spacecraft. As with drag, the detailed shape model was reduced to a sphere for this case study. The solar radiation pressure accelerations of the spacecraft for the truth and the nominal spherical shape model are shown in Figure 7, as well as the acceleration differences decomposed into a frame oriented along the Spacecraft-Sun line. Gaps in the time series occur when the spacecraft is behind Mars. The truth acceleration oscillates between 8.8e−5 mm/s^2 and 9.4e−5 mm/s^2 and averages near 9.15e-5 mm/s^2 while the simple model acceleration is constant near 9.18e-

© 2016. All rights reserved.

5 mm/ s^2. Recall, a sphere cannot capture the surface normal solar radiation pressure component which is the source of the oscillatory behavior; however, the sphere still captures the most significant portion of the acceleration as observed in Figure 7. Indeed, the differences in the accelerations are about an order of magnitude smaller than the absolute acceleration levels indicating the sphere is a reasonable approximation.

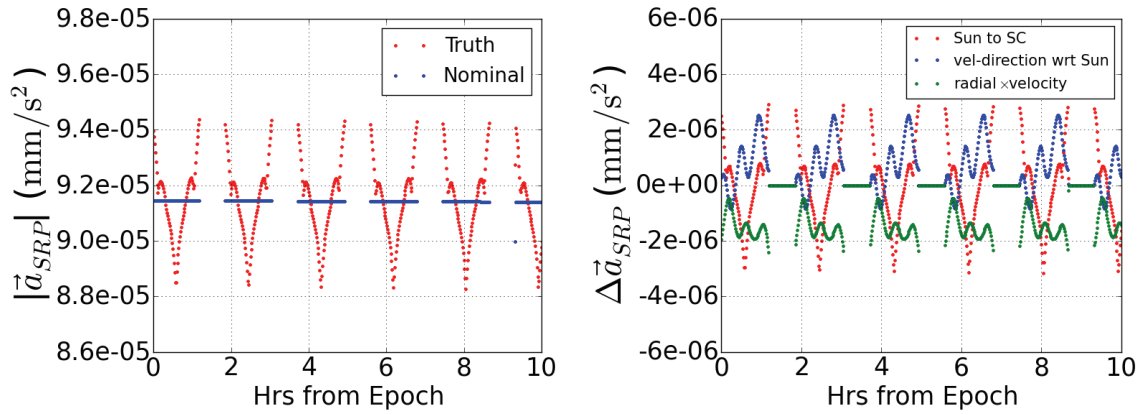

Figure 7: SRP accelerations values (left) for truth (red) and nominal with a spherical shape model (blue) and their differences (right).

Because of the gaps in the solar pressure introduced by Mars occultations, it is not feasible to compute a reliable Allan deviation. Rather, the process noise strength parameters were obtained via examining the standard deviation of the acceleration differences, and, as with drag, multiplying those levels by two. The process noise was also set to an ECRV with a correlation time of half an orbit to account for the presence of the occultations. Furthermore, the acceleration noise states were decomposed into a frame aligned with the Spacecraft-Sun vector, since for a sphere all SRP acceleration will be aligned with this line. The process noise will account for the unmodeled effects in the directions along this line as well as orthogonal to it. Again, all injected errors in the truth have been turned off, and the only error between truth and nominal is from the SRP model differences. The RSS of the filter position errors and associated uncertainties are shown in Figure 8. Note that as compared to the previous case with drag modeling simplifications, the filter errors and uncertainties for solar pressure model simplifications are much smaller with a steady state position error of 5 cm and uncertainty of 12 cm.

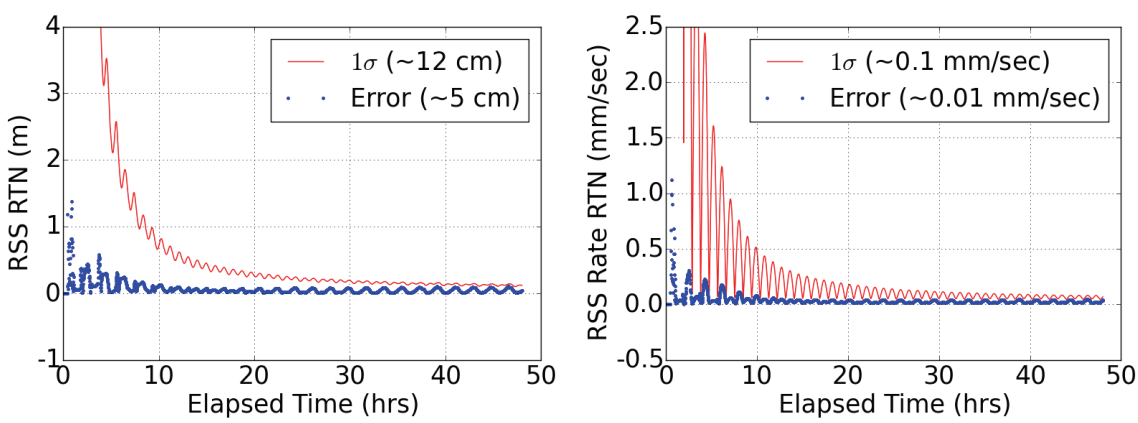

© 2016. All rights reserved.

Figure 8: Filter solution performance for position (left) and velocity (right) when modeling the spacecraft shape as a sphere for solar radiation pressure.

Gravitational Acceleration Reduced Model Fidelity Results

Three reduced gravity fields were examined with the spherical harmonic degrees and orders equal to {60,60}, {40,40}, and {10,10} and compared to the truth field with degree and order {95,95}. The gravity acceleration magnitudes for all cases oscillate between 0.6 cm/s^2 and 1.6cm/s^2 (including truth). More informative is provided via an examination of the acceleration differences of these three fields with truth. These are displayed in Figure 9 with the differences resolved into orbit radial, transverse, and normal (RTN) coordinates. Note the axes are all set equal to illustrate the increasing magnitude of the differences as the field size decreases. Typical magnitudes of the differences are 1e−3 mm/s^2, 6.9e−3 mm/s^2, and 1.5e−1 mm/s^2, respectively. Note that these acceleration differences are significantly larger than with either the drag or SRP cases, indicating this model simplification will dominate the performance of the filter.

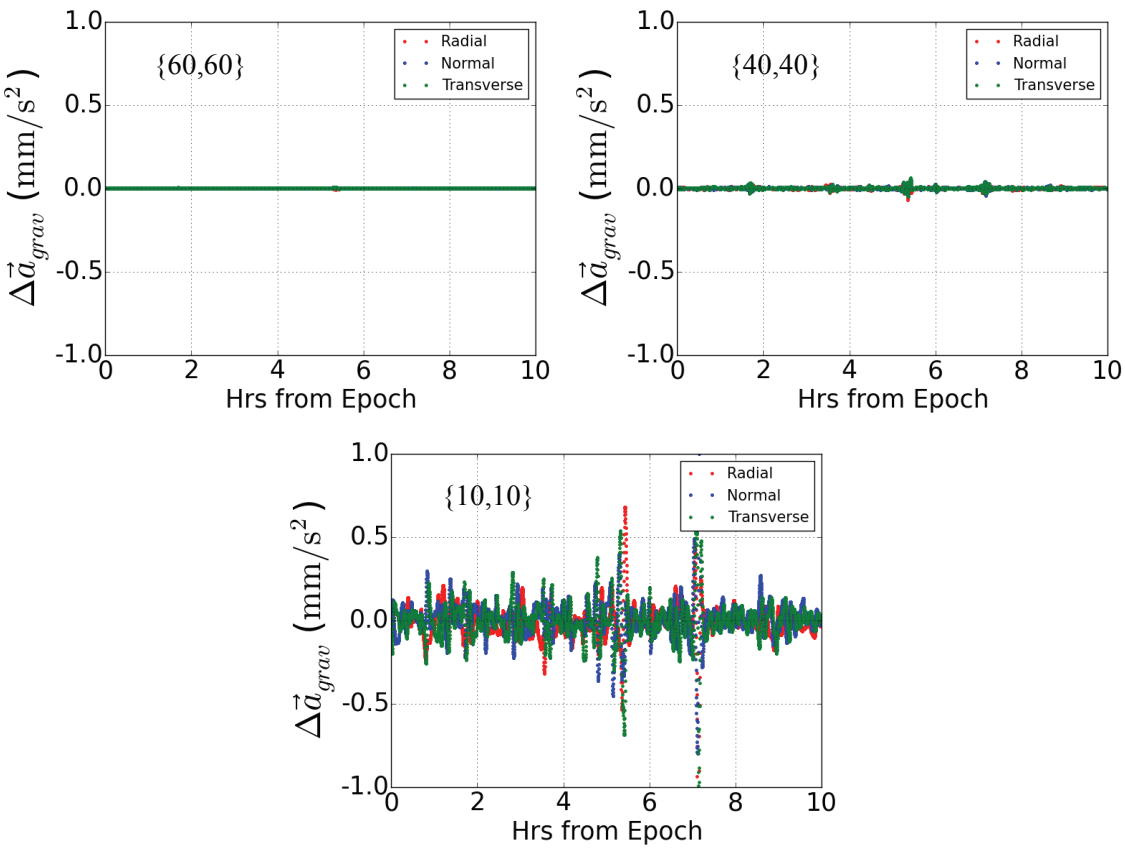

Figure 9: Differences of the truth gravity field with respect to {60,60} (upper left), {40,40} (upper right), and {10,10} (lower) fields expressed in a RTN frame.

The Allan deviations for these differences are displayed in Figure 10. Their slopes fall off as $1/\tau$, which is indicative of white phase noise. The filter's acceleration process noise models have been set to replicate this white noise behavior, with the uncertainty noise strength at two times the standard deviation of the acceleration differences for each case. For lower values of τ, the Allan deviation plots indicate a more complex noise behavior that differs from white, again, the factor of two is present to account for these effects.

© 2016. All rights reserved.

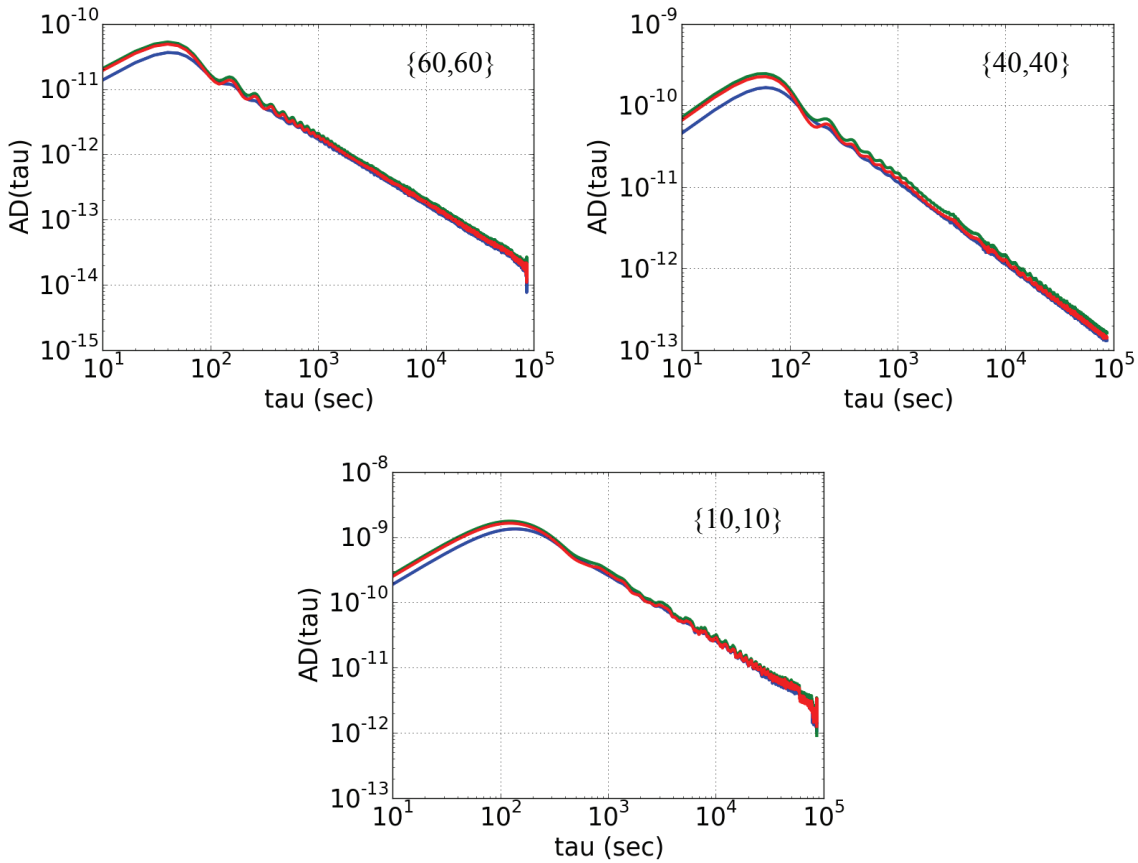

Figure 10: Allan deviations of the RTN gravity acceleration differences for the {60,60} (upper left), {40,40} (upper right), and {10,10} (lower) fields.

The RSS filter position errors are shown in Figure 11. The RMS of the filter solution errors were computed with the following results:

1. 60x60 gravity field position error RMS of 9m and velocity error RMS of 5mm/s.
2. 40x40 gravity field position error RMS of 29m and velocity error RMS of 2cm/s.
3. 10x10 gravity field position error RMS of 800m and velocity error RMS of 40cm/s, and note that this case did not reach convergence in a single iteration.

These results show that a transition between convergent solutions to non-convergent solutions was passed in reducing from a 40x40 field to a 10x10 field. The 60x60 field and 40x40 fields are considered further when examining the filter performance when all of the simulation errors are present and the results are compared to the orbit error requirements.

© 2016. All rights reserved.

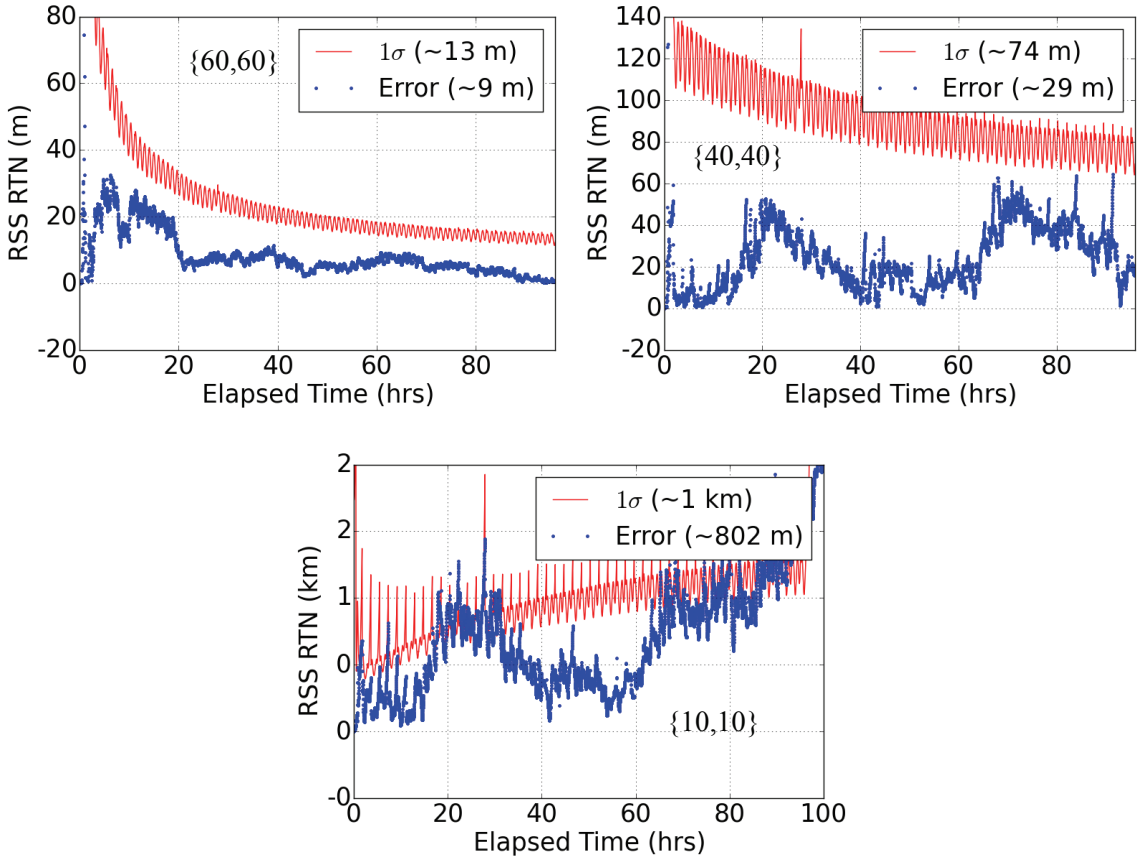

Figure 11: Filter position errors and uncertainties for the three reduced gravity field cases {60,60} (upper left), {40,40} (upper right), and {10,10} (lower).

To better characterize the expected filter performance limitations due to a reduced spherical harmonics field, additional cases were run. The RMS of the acceleration differences between the truth and nominal cases are shown in Figure 12. The values follow a linear trend on a logarithmic scale. This log behavior coupled with the empirical factor of two can be utilized as a guide for selecting process noise strength that yields satisfactory filter solutions for different gravity field sizes past the 10x10. Indeed, the case for the 13x13 field (not shown) yields convergent filter solutions. This field size includes the dominant tesseral effects that MRO samples on every orbit; hence, may represent a minimal field size that produces satisfactory filter solutions for this orbit.

© 2016. All rights reserved.

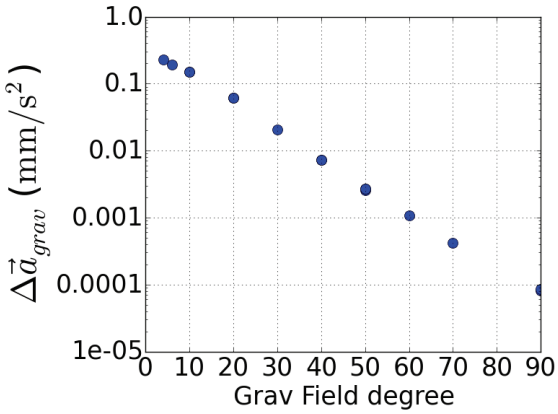

Figure 12: RMS of (truth-nominal) gravity accelerations varying gravity degree values.

Comparing The Model Simplifications

It is illustrative to compare the position and velocity filter solution errors for all cases as shown in Table 2.

Table 2: Comparison of the cases

Case	RMS Pos Err	RMS Vel Err	Accel Mag (km/s^2)	Accel Diff (km/s^2)
Grav 10x10	800 m	40 cm/s	0.6e-6 to 1.6e-6	1.5e-7
Grav 40x40	29 m	1.5 cm/s	0.6e-6 to 1.6e-6	6.9e-9
Grav 60x60	9 m	4 mm/s	0.6e-6 to 1.6e-6	1e-9
Drag Sphere SC	33 cm	0.2 mm/s	1.7e-10	6e-10
Drag Sphere SC & Simple Atm	42 cm	0.3 mm/s	1.7e-10	9e-10
SRP Sphere SC	5 cm	0.03 mm/s	7e-11	4e-12

The simplification of the gravity field had the greatest effect on the filter performance, followed by drag, and then SRP. Next was the simplified drag model. It should be noted that the two drag models had similar results, which indicates the fidelity of the atmospheric density model does not significantly affect the filter performance (at least for reconstruction). Table 2 also shows that the magnitude of the solution error is correlated with both the magnitude of the acceleration as well as the difference in acceleration between the high fidelity and simplified models.

Combined Result with All Errors and Model Simplifications

We are in a position now to examine the performance of the filter when using all of the model simplifications discussed and in the presence of all the injected truth model errors turned on as specified in Table 1. Recall that the objective was to determine a set of model simplifications that reduce computational complexity yet are still able to produce orbit solutions meeting the orbit accuracy requirements presented earlier. Specifically, satisfy 0.5m in the radial direction, 33m in the transverse direction, and 13m in the cross-track direction. The selected model simplifications are delineated in Table 3.

© 2016. All rights reserved.

Table 3: Selected Model Simplifications

1. Reduce the Mars gravity field to a degree and order of 60 x 60 (note that the smaller 40x40 field violated the requirements)
2. Use the simplified MarsGs density with parameters selected with a best fit to the high fidelity MarsGRAM 2005 density over the span of the simulation
3. Use a spherical spacecraft shape model selected to minimize the deviations with the high fidelity drag accelerations when using the simplified density
4. Use a second spherical spacecraft shape tuned to minimize deviations with the high fidelity solar radiation pressure accelerations.

The results of the simulation are presented in Figure 13 with the errors and uncertainties separated into their radial, transverse, and normal components.

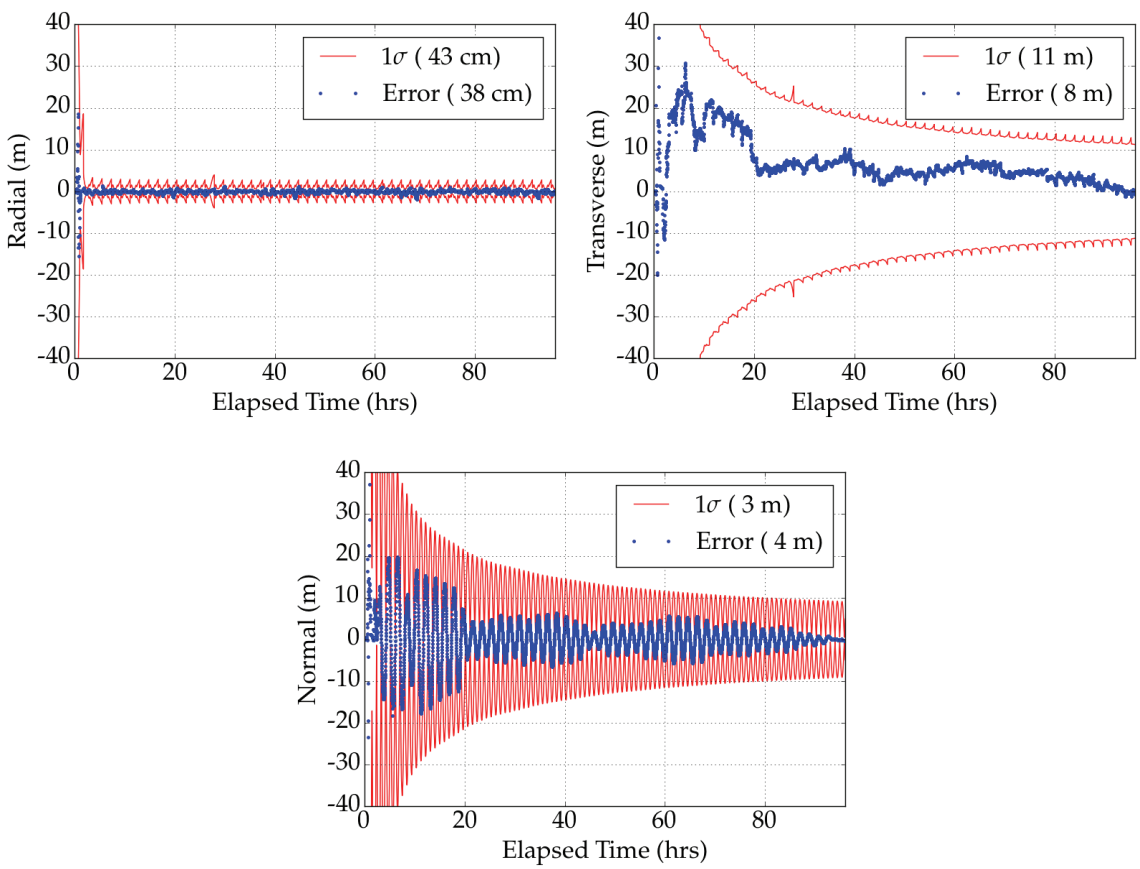

Figure 13: Reduced model filter solution results expressed in RTN components.

The RMS of the steady-state solution errors are 38 cm in radial direction, 8 m in the transverse direction, and 5 m in the cross-track direction. The filter succeeds with 98 percent of the points within the one sigma bound indicating that it's well-tuned. Finally, these error levels also satisfy the orbit requirements. A further simplification to a 50 x 50 gravity field was conducted and shown to meet the requirements in the transverse and normal directions, but violate the radial direction

© 2016. All rights reserved.

requirement - coming in at a 90 cm error. Thus, use of the models identified in Table 3 has yielded a minimally sufficient set of simplifications that satisfy the stated requirements.

Extended Kalman Filter Investigation

Recall, that the initial condition errors in the previous results were restricted to 5 cm and 5 mm/s (1σ) because the LKF solutions became biased when initial position and velocity errors were larger than these levels. Operationally the LKF processing is iterated so that larger initial condition errors can be admitted; however, this could be computationally expensive for an onboard implementation. Another strategy that we explore here is to adapt the processing to use an Extended Kalman Filter as this may eliminate the need to iterate and its associated computational cost. The EKF approach investigated is an extension of the typical EKF that rectifies the nonlinear orbit with the solution from the filter after processing each measurement. In particular, the user can choose to rectify after a processing a selected number of measurements. During processing within the interval of the specified measurement set, the EKF actually behaves like a LKF. Rectification occurs after processing the measurement set and then proceeds to the next interval of measurements. The objective here is to explore the initial condition error bounds that are admissible and still yield statistically convergent solutions.

We begin by examining results using the full fidelity truth models as outlined previously; however, with all injected truth errors turned off except for initial condition errors. Additionally, since there are only initial condition (I.C.) errors, all filter process noise states have been turned off so that only position and velocity components are being estimated. The filter has also been configured in the traditional manner to rectify after processing each measurement. The initial condition errors have been examined at three different levels with random initialization of position component errors at 100 m, 1000 m, and 10000 m (1σ). The velocity components were all randomly initialized using 1 mm/s (1σ) errors. Furthermore, five different random seeds were examined to ensure any given realization does not skew the results and conclusions. To determine if the filter was producing statistically convergent solutions, the solution errors were compared with the associated 1σ-uncertainties and a percent exceedance was computed. A properly convergent filter should yield exceedances no more than 32% of the time; anything larger suggests a biased or divergent solution. The results have been tabulated in Table 4 when only initial condition errors are active.

Table 4: EKF Solution Exceedance Rates with Only I.C. Errors

I.C. Error (1σ)	Seed 1 Exceedances	Seed 2 Exceedances	Seed 3 Exceedances	Seed 4 Exceedances	Seed 5 Exceed-ances
100 m	0 %	0 %	0 %	0 %	0 %
1,000 m	0 %	0 %	0 %	0 %	0 %
10,000 m	6.9 %	0 %	69.2 %	0 %	19.7 %

Except for the singular case at 10,000 m (1σ) errors with Seed 3, all the solutions have yielded convergent, unbiased results. This suggests that the EKF should be able to expand the allowable initial condition error bounds to at least 1 km versus the LKF case with only 5 cm. A definite improvement; however, does this performance persist when the other errors are injected back into the simulation?

In the next set of results, the baseline results are revisited and the initial condition errors have been increased to 100 m (1σ). The results are tabulated for the five different seeds in Table 5.

© 2016. All rights reserved.

Table 5: EKF Solution Exceedance Rates with All Errors

I.C. Error (1σ)	Seed 1 Exceedances	Seed 2 Exceedances	Seed 3 Exceedances	Seed 4 Exceedances	Seed 5 Exceedances
100 m	16.9 %	97.1 %	19.7 %	97.2 %	42.5 %

Now the EKF is unable to consistently achieve convergent, unbiased solutions even with the modest 100 m initial condition errors. There may be smaller initial condition errors (which are still greater than the 5 cm levels) that work, but a robust approach should allow for initial errors that are at least a 100 m (and most likely larger). The expansion of the EKF to process more than one measurement before rectification did not improve the situation. Thus, use of an EKF is not recommended for an onboard, autonomous application that must be able to start with large uncertainties in the initial trajectory – a different strategy is required. There may still be options for use of an EKF that employs starting with an initial orbit determination routine (such as Gauss's method) to get starting errors for the EKF within a reasonable bound, or use of an iterated LKF might be required. This is to be explored in future work.

CONCLUSION

This study has found three significant model simplifications for a Mars orbit determination problem yielding a sub-optimal filter that still produces satisfactory orbit solution accuracies. In particular, a reduction in the gravity field size, simplification of a spacecraft shape to a sphere, and use of a simplified Mars atmosphere model produce noticeable computational efficiencies. These could be considered for use in an onboard orbit determination system when processing one-way radiometric tracking with the data quality afforded by DSAC. It was also found that initial condition errors present a difficulty for robust onboard filter operation, and that a typical EKF implementation might not be well suited for solving this problem. Future work will explore augmentations to the EKF or alternatives that admit a robust filter initialization. Additionally, quantifying the computational performance improvements and sizing for an onboard implementation is a key next step.

ACKNOWLEDGEMENTS

This research was carried out at the Jet Propulsion Laboratory, California Institute of Technology, under a contract with the National Aeronautics and Space Administration.

REFERENCES

[1] T. A. Ely, J. Seubert, and J. Bell, "Advancing Navigation, Timing, and Science with the Deep-Space Atomic Clock," *Space Operations: Innovations, Inventions, and Discoveries*, American Institute of Aeronautics and Astronautics, Inc., 2015, pp. 105–138.

[2] J. E. Riedel, S. Bhaskaran, P. N. Desai, D. Han, B. Kennedy, G. W. Null, S. P. Synnott, T. C. Wang, R. A. Werner, E. B. Zamani, T. McElrath, and M. Ryne, "Deep Space 1 Technology Validation Reports: Autonomous Optical Navigation," no. JPL Publication 00–10, No. 1. NASA, 1999.

[3] D. G. Kubitschek, N. Mastrodemos, R. A. Werner, S. P. Synnott, S. Bhaskaran, J. E. Riedel, B. M. Kennedy, G. W. Null, and A. T. Vaughan, "The Challenges of Deep Impact Autonomous Navigation," *J. F. Robot.*, vol. 24, no. 4, pp. 339–354, 2007.

[4] S. Bhaskaran, "Autonomous Navigation for Deep Space Missions," in *12th International Conference on Space Operations*, 2012.

© 2016. All rights reserved.

[5] T. A. Ely and J. Seubert, "One-Way Radiometric Navigation with the Deep Space Atomic Clock," in *AAS/AIAA Space Flight Mechanics Meeting*, 2015.

[6] T.-H. You, A. Halsell, E. Graat, S. Demcak, D. Highsmith, S. Long, N. Mottinger, E. Higa, and M. Jah, "Navigating Mars Reconnaissance Orbiter: Launch Through Primary Science Orbit," in *AIAA Space 2007 Conference and Exposition*, 2007.

[7] M. T. Zuber, F. G. Lemoine, D. E. Smith, A. S. Konopliv, S. E. Smrekar, and S. W. Asmar, "Mars Reconnaissance Orbiter Radio Science Gravity Investigation," *J. Geophys. Res.*, vol. 112, no. E5, p. E05S07, May 2007.

[8] H. L. Justh and C. G. Justus, "MARS GLOBAL REFERENCE ATOMSPHERIC MODEL (Mars-GRAM 2005) APPLICATIONS FOR MARS SCIENCE LABORATORY MISSION SITE SELECTION PROCESSES," in *7th International Conference on Mars*, 2007.

[9] M. A. Vincent, "Explanation and History of the New Solar Cycle/Atmospheric Model Used in Mars Planetary Protection Analysis," in *Advances in the Astronautical Sciences, Vol. 109*, 2001, pp. 1599 – 1614.

[10] M. A. Vincent, T. A. Ely, and T. H. Sweetser, "Plan and Progress for Updating the Models Used for Orbiter Lifetime Analysis," in *Advances in the Astronautical Sciences, Vol. 142*, 2011, pp. 1835 – 1849.

[11] T. A. Ely, "Mean Element Propagations Using Numerical Averaging," *J. Astronaut. Sci.*, vol. 61, no. 3, pp. 275–304, Dec. 2014.

[12] J. A. Davis, C. A. Greenhall, and P. W. Stacey, "A Kalman filter clock algorithm for use in the presence of flicker frequency modulation noise," *Metrologia*, vol. 42, no. 1, pp. 1–10, Feb. 2005.

© 2016. All rights reserved.